Chemical Science

ROYAL SOCIETY OF CHEMISTRY

EDGE ARTICLE

View Article Online
View Journal | View Issue

Cite this: *Chem. Sci.*, 2024, **15**, 18187

All publication charges for this article have been paid for by the Royal Society of Chemistry

A multi-functional protective material with atomically dispersed zincophilic sites enabling long-life zinc anodes†

Miaomiao Zhang,‡[a] Hongyu Wei,‡[a] Yitong Zhou,*[b] Weidong Wen,[ac] Lin Zhang*[c] and Xin-Yao Yu *[a]

Received 3rd July 2024
Accepted 30th September 2024

DOI: 10.1039/d4sc04385e

rsc.li/chemical-science

Parasitic side reactions and the formation of zinc dendrites in aqueous solutions severely hinder the practical application of Zn metal anodes. Carbon materials with high electrical conductivity and mechanical robustness are promising protective materials for Zn anodes. However, the zincophobic nature of carbon materials impedes the cycling stability of zinc-ion batteries. Herein, a versatile design strategy is proposed utilizing carbon doped with single atoms with atomically dispersed zincophilic sites as a multi-functional protective material for high-performance zinc anodes. Taking bismuth-single-atom-doped carbon (Bi SAs) as an example, density functional calculations verify that the introduction of bismuth single atoms can enhance zincophilicity, promote robust adhesion to zinc foil, and effectively suppress hydrogen evolution. Guided by theoretical calculations, Bi single-atom-doped carbon nanobelts are synthesized and employed as a protective material to stabilize zinc anodes. As expected, due to the atomic-level zincophilic Bi sites, hydrophobicity, and enhanced ionic conductivity, the Bi SAs@Zn anode demonstrates over 4200 h and 600 h of reversible cycling at 5 mA cm^{-2} and 20 mA cm^{-2}, respectively, in symmetric cells. Additionally, the Bi SAs@Zn//MnO_2 full cell achieves a stable lifespan of 1000 cycles at 1 A g^{-1}, retaining 95.58% of the initial capacity.

Introduction

Aqueous zinc-ion batteries are recognized as highly promising contenders for sustainable energy storage based on their cost-effectiveness, outstanding safety features, environmental friendliness, and potential for scalable production.[1,2] Zn metal anodes offer several inherent advantages, including a high theoretical capacity (820 mA h g^{-1}) and low redox potential (−0.76 V *vs.* standard hydrogen electrode).[3,4] However, the practical application of Zn anodes is severely hindered by their poor cycling stability and low coulombic efficiency (CE), which result from deleterious side reactions such as the hydrogen evolution reaction (HER), Zn corrosion, and by-product formation, as well as dendrite growth.[5–8]

To tackle the challenges of Zn anodes, various strategies have been developed, such as constructing protective layers,[9–12] designing three-dimensional (3D) current collectors,[13] and optimizing functional electrolytes.[14–17] Among these approaches, the coating of a protective layer on the zinc surface is regarded as an effective method for mitigating the HER and promoting uniform Zn deposition.[18,19] To date, various zinc protective materials have been explored, including carbon materials,[20] metal oxides,[21,22] metal–organic frameworks,[23] and organic compounds.[24] Among these materials, carbon materials have garnered significant attention due to their outstanding conductivity and excellent mechanical robustness.[25] For instance, Mai *et al.* demonstrated that an interfacial layer composed of carbon nanotubes could effectively modulate the local current density, ensuring a dendrite-free zinc anode.[26] However, the inherent zincophobic nature of carbon materials leads to a high Zn nucleation barrier and poor adhesion of the protective layers to the zinc anodes.[20,27] Therefore, it is of great importance to increase the zincophilic sites of carbon materials and thus to enhance their performance in the protection of zinc anodes.

Single atoms (SAs)-doped materials with atomically dispersed metal sites have been widely investigated in various fields due to their homogeneous reactive sites and high utilization efficiency of the metal.[28,29] In recent years, SAs with atomic scale lithiophilic sites have been investigated as hosts or protective layers for high-performance lithium metal batteries.[30–33] For example, Guo *et al.* found that an atomically

[a]*School of Materials Science and Engineering, Anhui University, Hefei 230601, P. R. China. E-mail: yuxinyao@ahu.edu.cn*

[b]*Institutes of Physical Science and Information Technology, Anhui University, Hefei 230601, P. R. China. E-mail: zhouyt@ahu.edu.cn*

[c]*Institute of Solid State Physics, Leibniz University Hannover, Hannover 30167, Germany. E-mail: lin.zhang@fkp.uni-hannover*

† Electronic supplementary information (ESI) available. See DOI: https://doi.org/10.1039/d4sc04385e

‡ These two authors contributed equally to this work.

dispersed cobalt coordinate conjugated bipyridine-rich covalent organic framework as an artificial solid electrolyte interphase (SEI) on the surface of Li metal anode can regulate the Li^+ local coordination environment and achieve uniform Li nucleation.[34] Most recently, SAs have been explored to improve the electrochemical performance of Zn metal anodes. For instance, Lou *et al.* reported an elaborate design with atomically dispersed Cu and Zn sites anchored on N,P-co-doped carbon macroporous fibers as a three-dimensional (3D) host for a zinc anode, presenting a low Zn nucleation overpotential, high reversibility, and dendrite-free Zn deposition.[35] Nevertheless, the application of SAs in zinc metal anode optimization is still in the early stage. In these studies, SAs are mainly employed to modify the zinc host or scaffold materials.[36–38] SAs are rarely applied as a protective layer for zinc anodes.[39] The protection mechanisms based on SAs also remain largely unexplored, but are very critical for designing high-performance zinc anodes.

In this work, we propose that single-atom-doped carbon with atomically dispersed zincophilic sites is an efficient protective material for zinc anodes. Considering bismuth (Bi) single atoms as an example, density functional theory (DFT) calculations first predict that Bi-single-atom-doped carbon (Bi SAs) exhibits greater zincophilicity and stronger adhesion to zinc foil than nitrogen-doped carbon (NC). The Bi SAs also exhibit hydrophobic properties and a greater ability to inhibit the HER. Inspired by the DFT predictions, Bi SAs nanobelts are synthesized and used as a protective material for a zinc anode. Excitingly, the Bi SAs@Zn anode achieves satisfactory electrochemical performance in symmetric, asymmetric, and full cells.

Results and discussion

DFT calculations are performed to investigate the feasibility of the application of Bi SAs as a protective layer for zinc anode. Atomic models of Bi SAs, NC, Bi metal, and bare Zn are first constructed (Fig. S1†). The nucleation energy barrier for Zn clusters at the zincophilic sites is then calculated. The nucleation energy barrier of the first Zn atom on the Bi SAs is 0.741 eV which is weaker than that of NC (0.860 eV) and Bi metal (0.857 eV) (Fig. S2a†), indicating that Bi SAs exhibit greater zincophilicity than NC and Bi metal. Although the nucleation energy barrier of the first Zn atom on the Bi SAs is slightly higher than that on bare Zn (0.645 eV), it is noteworthy that the chemical potential of Zn deposition on bare Zn from the second Zn atom on decreases sharply (Fig. 1a), which is unfavorable for

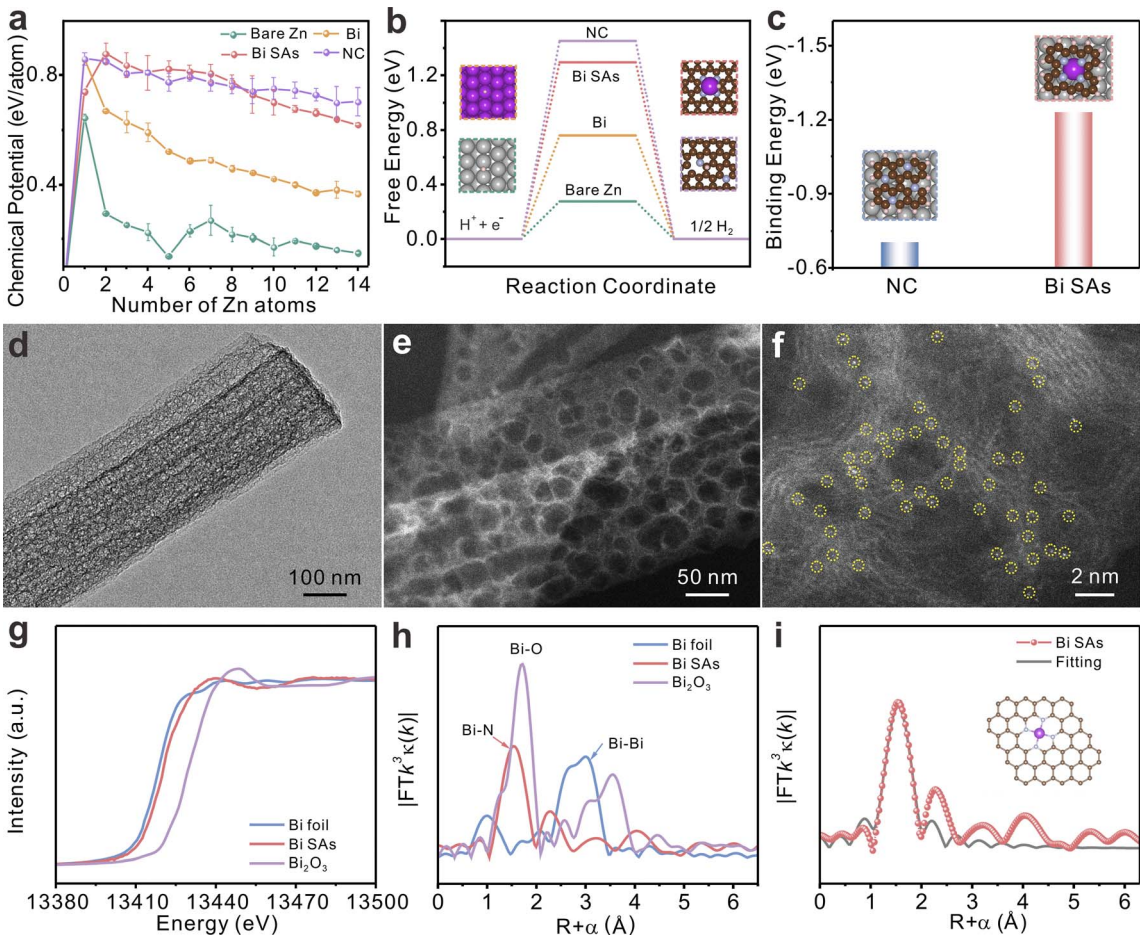

Fig. 1 (a) Changes in the chemical potential of bare Zn, Bi SAs, Bi, and NC for zinc cluster nucleation. (b) Hydrogen adsorption Gibbs free energy diagram of bare Zn, Bi SAs, Bi, and NC. (c) Binding energy of NC and Bi SAs on bulk Zn. (d) TEM image, (e) STEM image, and (f) aberration-corrected HAADF-STEM image of Bi SAs. (g) Bi L_3-edge XANES and (h) FT-EXAFS spectra of Bi foil, Bi SAs, and Bi_2O_3. (i) EXAFS fitting of Bi SAs.

homogeneous Zn nucleation. A similar phenomenon can be also observed on Bi metal. In contrast, the Bi SAs and NC surfaces maintain a relatively stable chemical potential during the deposition of successive Zn atoms. As illustrated, by the deposition of the 14th Zn atom (Fig. S2b†), both Bi SAs and NC are conductive for the uniform nucleation and growth of Zn. Fig. 1b shows that the calculated Gibbs free energies for hydrogen adsorption on Bi SAs (1.30 eV), NC (1.45 eV), and Bi metal (0.76 eV) are higher than that on bare Zn (0.28 eV), suggesting that Bi SAs exhibit great potential to hinder the HER. In addition, an ideal artificial protective layer should exhibit strong adhesion to zinc foil to prevent coating delamination during cycling. Compared to that of NC (−0.70 eV), Bi SAs demonstrate a much stronger binding energy of −1.22 eV to zinc foil (Fig. 1c), which can not only inhibit coating delamination but also promote efficient electron transfer between the coating layer and zinc foil.

Guided by these DFT simulations, a straightforward pyrolysis strategy[40] is employed to synthesize Bi single atoms-doped carbon nanobelts using a Bi metal–organic framework as a template (Fig. S3†). The as-synthesized material exhibits an amorphous carbon structure and belt-like morphology (Fig. S4†). The nanobelts are highly porous, as confirmed by transition electron microscopy (TEM) and high-angle annular dark-field scanning transmission electron microscopy (HAADF-STEM) images (Fig. 1d and e). The porous structure is expected to facilitate rapid ion transport. Isolated bright spots (marked with yellow circles) can be clearly observed in the aberration-corrected HAADF-STEM image (Fig. 1f), evidencing the existence of Bi single atoms. The Bi content is determined to be 1.56 wt% using inductively coupled plasma-optical emission spectrometry (ICP-OES).

X-ray photoelectron spectroscopy (XPS) is performed to study the chemical state of the as-synthesized material. The four peaks of the C 1s XPS spectra can be assigned to C=C (284.8 eV), C=N (286.1 eV), C–N (288.5 eV), and O–C=O (290.5 eV) species (Fig. S5a†). The high-resolution N 1s spectrum can be deconvoluted into graphitic N and pyridinic N (Fig. S5b†). The Bi 4f XPS spectrum shows a valence state between 0 and 3 (Fig. S5c†). Furthermore, the accurate local atomic coordination of Bi SAs is determined using X-ray absorption near-edge spectroscopy (XANES) and extended X-ray absorption fine

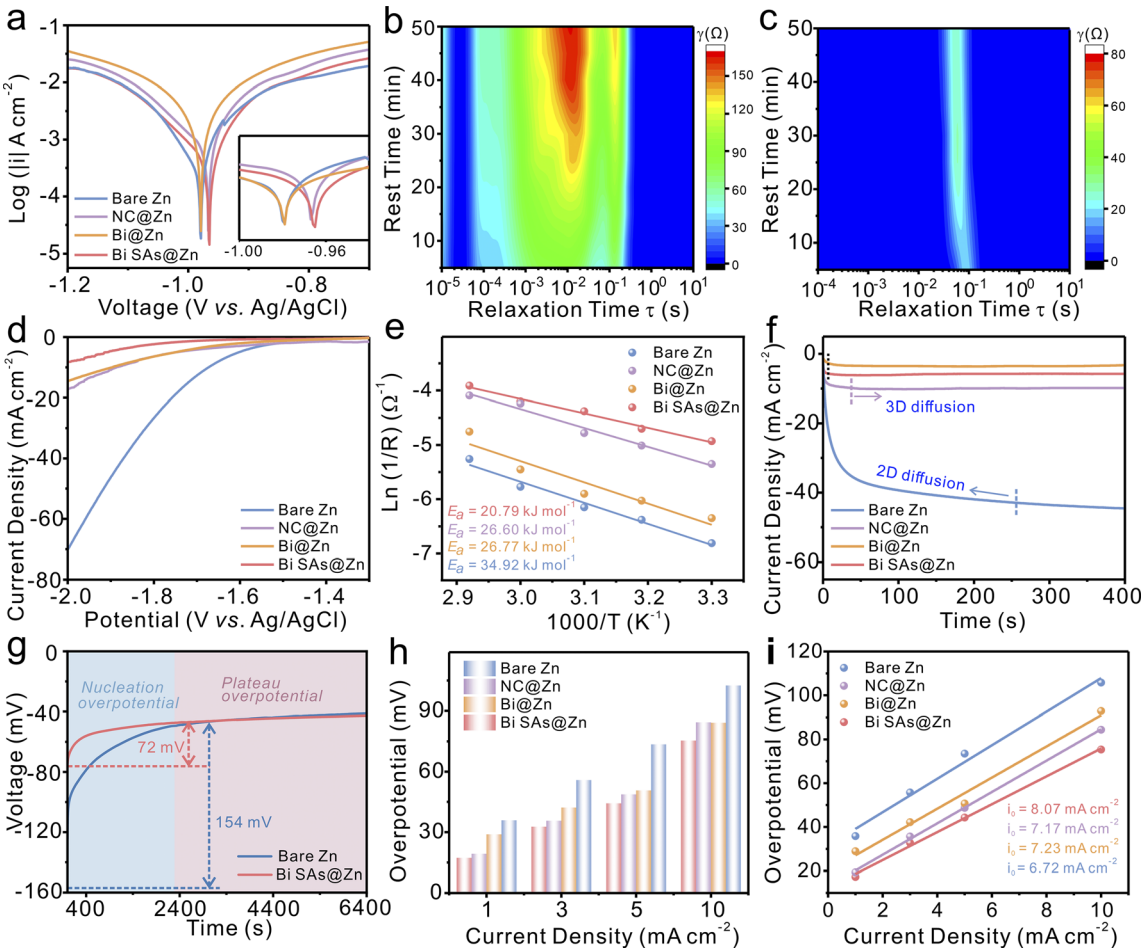

Fig. 2 (a) Tafel curves of bare Zn, NC@Zn, Bi@Zn and Bi SAs@Zn electrodes in 2 M $ZnSO_4$ electrolyte. DRT analysis of (b) bare Zn and (c) Bi SAs@Zn in symmetric cells during standing by EIS. (d) LSV curves in 1 M Na_2SO_4 electrolyte, (e) activation energies, and (f) CA curves at an overpotential of −150 mV. (g) Nucleation overpotential of bare Zn and Bi SAs@Zn electrodes at a current density of 5 mA cm^{-2} in 2 M $ZnSO_4$ electrolyte. (h) Overpotential plots at different current densities and the corresponding (i) exchange current density of bare Zn, NC@Zn, Bi@Zn, and Bi SAs@Zn electrodes.

structure spectroscopy (EXAFS). As depicted in Fig. 1g, the Bi L_3-edge XANES spectrum of the as-synthesized material is located between that of Bi foil and Bi_2O_3, demonstrating that the average valence of the Bi in the as-synthesized material is between Bi^0 and Bi^{3+}, consistent with the XPS results. The Fourier transform (FT) EXAFS spectrum of the as-synthesized material in Fig. 1h exhibits a dominant Bi–N coordination at 1.47 Å. Moreover, there are no detectable peaks for Bi–Bi coordination, implying that the Bi atoms are dispersed as isolated atoms. The EXAFS fitting results affirm the coordination structure of the Bi sites as Bi–N_4 (Fig. 1i and Table S1†). The above characterization results show that Bi-single-atom-doped carbon nanobelts are successfully synthesized; the product is henceforth referred to as Bi SAs. As control samples, NC and bulk Bi are also synthesized (Fig. S6 and S7†).

All the synthesized materials are then coated onto Zn foil to evaluate their Zn protection performance. Fig. 2a illustrates that the Bi SAs@Zn electrode exhibits a more positive corrosion potential than the NC@Zn, Bi@Zn, and bare Zn electrodes, indicating that Bi SAs is effective in inhibiting the corrosion of zinc metal. This may be due to the hydrophobic properties and low SO_4^{2-} permeability of the Bi SAs surface (Fig. S8 and S9†). When bare Zn and Bi SAs@Zn electrodes are immersed in 2 M $ZnSO_4$ solution for three days, white precipitates with an inhomogeneous flaky structure, corresponding to $Zn_4SO_4(OH)_6 \cdot xH_2O$, form on the surface of bare Zn, while no significant changes are observed on Bi SAs@Zn (Fig. S10†). *In situ* electrochemical impedance spectroscopy (EIS) is performed to further investigate the corrosion resistance performance through analyzing the distribution of relaxation time (DRT).[41] A new peak appears in the DRT of bare Zn after 40–50 minutes of resting, indicating the formation of by-product (Fig. 2b and S11a†). In sharp contrast, no obvious peak can be found for Bi SAs@Zn (Fig. 2c and S11b†). Additionally, the linear sweep voltammetry (LSV) curves in Fig. 2d illustrate that much higher overpotentials are required for Bi SAs@Zn to trigger the HER, suggesting the significant HER suppression properties of Bi SAs.

The ionic conductivity of the Bi SAs interfacial layer is determined to be as high as 2.42×10^{-3} S cm^{-1} (Fig. S12†), further validating the effective role of Bi single atoms in accelerating Zn^{2+} transport. As determined using the Arrhenius

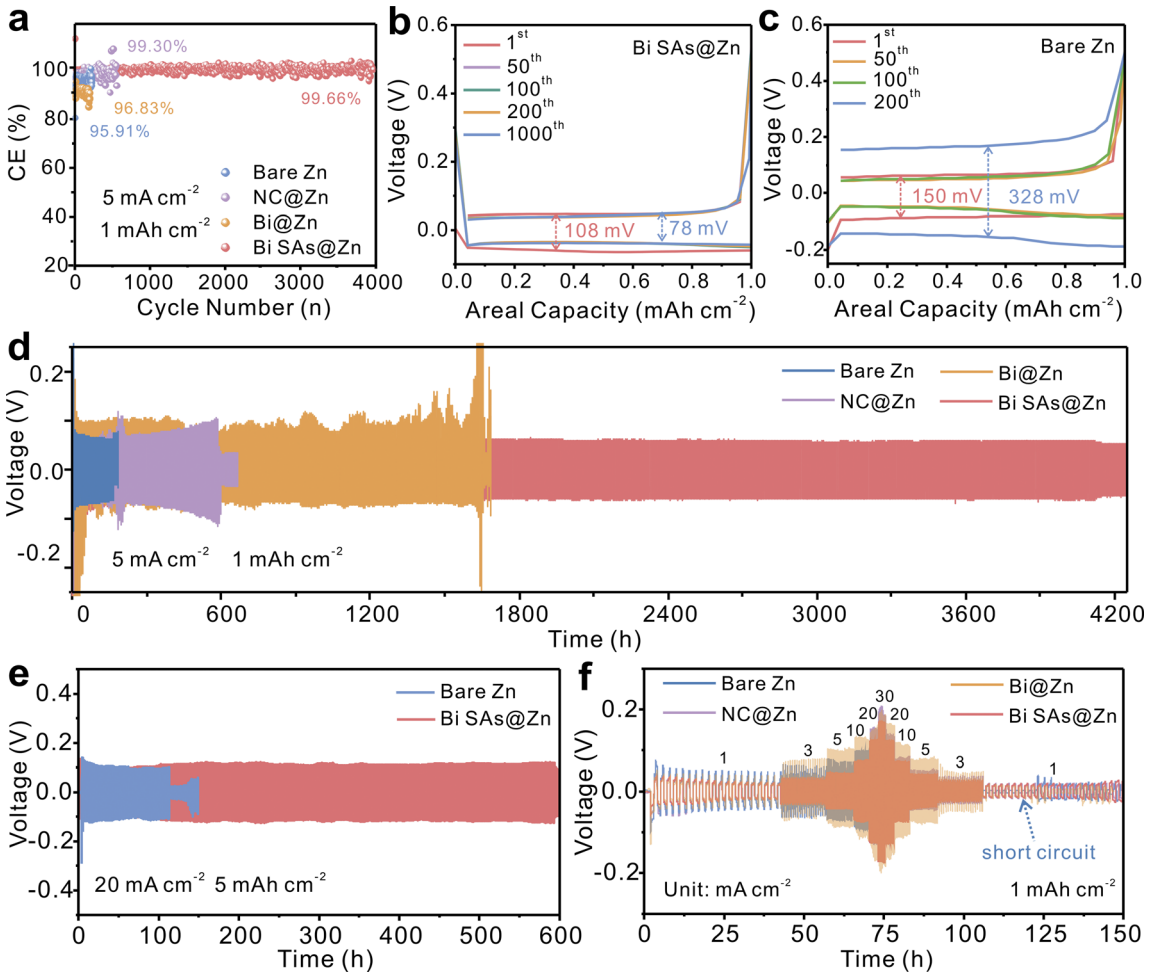

Fig. 3 (a) CE profiles of Zn//Ti, NC@Zn//Ti, Bi@Zn//Ti and Bi SAs@Zn//Ti at 5 mA cm^{-2} and 1 mAh cm^{-2}. Galvanostatic charge/discharge curves of (b) Bi SAs@Zn//Ti and (c) Zn//Ti. (d) Long-term cycling stability of bare Zn, NC@Zn, Bi@Zn, and Bi SAs@Zn symmetric cells at 5 mA cm^{-2} and 1 mAh cm^{-2}. (e) Cycling stability at 20 mA cm^{-2} and 5 mAh cm^{-2} and (f) rate performance at different current densities from 1 to 30 mA cm^{-2} of bare Zn and Bi SAs@Zn.

equation (Fig. 2e and S13†), the activation energy (E_a) for Bi SAs@Zn (20.79 kJ mol^{-1}) is lower than that of NC@Zn (26.60 kJ mol^{-1}), Bi@Zn (26.77 kJ mol^{-1}), and bare Zn (34.92 kJ mol^{-1}), which may be attributed to the high surface energy of the single atoms in promoting Zn^{2+} desolvation and migration.[42] With the exception of the bare Zn anode, the other electrodes initially exhibit a rapid 2D diffusion process (within 10 s), followed by a stable 3D diffusion phase (Fig. 2f), demonstrating uniform Zn deposition. The nucleation overpotential of Bi SAs@Zn (72 mV) is much smaller than that of bare Zn (154 mV) (Fig. 2g), suggesting that less energy is required for nucleation on Bi SAs. Within the examined current density range (1 to 10 mA cm^{-2}), the observed overpotentials of Bi SAs@Zn are consistently lower than those of NC@Zn, Bi@Zn, and bare Zn (Fig. 2h). In addition, the exchange current density of Bi SAs@Zn is higher than that of the other three electrodes, reflecting that Bi SAs can promote surface charge transfer kinetics (Fig. 2i).

The Zn^{2+} plating/stripping behaviors are investigated in both asymmetric and symmetric cells. As depicted in Fig. 3a, the Bi SAs@Zn//Ti cell can maintain an average CE of 99.66% over 4000 cycles at a current density of 5 mA cm^{-2} with a capacity of 1 mAh cm^{-2}, demonstrating remarkable reversibility and stability. As evidenced by the voltage–capacity profiles, the Bi SAs@Zn//Ti cell displays a well-leveled charging–discharging plateau with a lower voltage gap throughout the entire cycling (Fig. 3b). In contrast, the voltage polarization of bare Zn//Ti increases sharply at the 200th cycle, which can be attributed to the formation of Zn dendrites (Fig. 3c). In addition, a high and stable CE is also exhibited by the Bi SAs@Zn//Ti cell at various current densities (Fig. S14 and S15†), while the Zn//Ti, NC@Zn//Ti, and Bi@Zn//Ti cells show an unstable CE and short cycle life. In the symmetric cell tests, the thickness of the coating layer is first optimized to be 5 μm (Fig. S16 and S17†). At 5 mA cm^{-2} and 1 mAh cm^{-2}, the Bi SAs@Zn symmetric cell can achieve a long lifespan of 4200 h without notable voltage fluctuations (Fig. 3d), much better than those of the NC@Zn, Bi@Zn, and bare Zn cells. Even tested at 20 mA cm^{-2} and 5 mAh cm^{-2}, the Bi SAs@Zn cell still presents superior cycling stability up to 600 h with a cumulative capacity as high as 6000 mAh cm^{-2} (Fig. 3e), again demonstrating the high durability and reversibility of Bi SAs@Zn. Remarkably, the cumulative capacity and cycle life of the Bi SAs@Zn anode outperform many previously reported Zn metal anodes (Table S2†). Moreover, at a high depth of discharge (DOD) of 85.47% (5 mA cm^{-2}, 10 mAh cm^{-2}), the Bi SAs@Zn cell displays an impressively long cycle life of 600 hours (Fig. S18†). Additionally, the rate performance tests reveal that the Bi SAs@Zn cell can deliver a smaller voltage hysteresis and better stability than the NC@Zn, Bi@Zn, and bare Zn cells under different current densities ranging from 1 mA cm^{-2} to 30 mA cm^{-2} (Fig. 3f). As elucidated by galvanostatic intermittent titration technique (GITT) tests, the Bi SAs can effectively

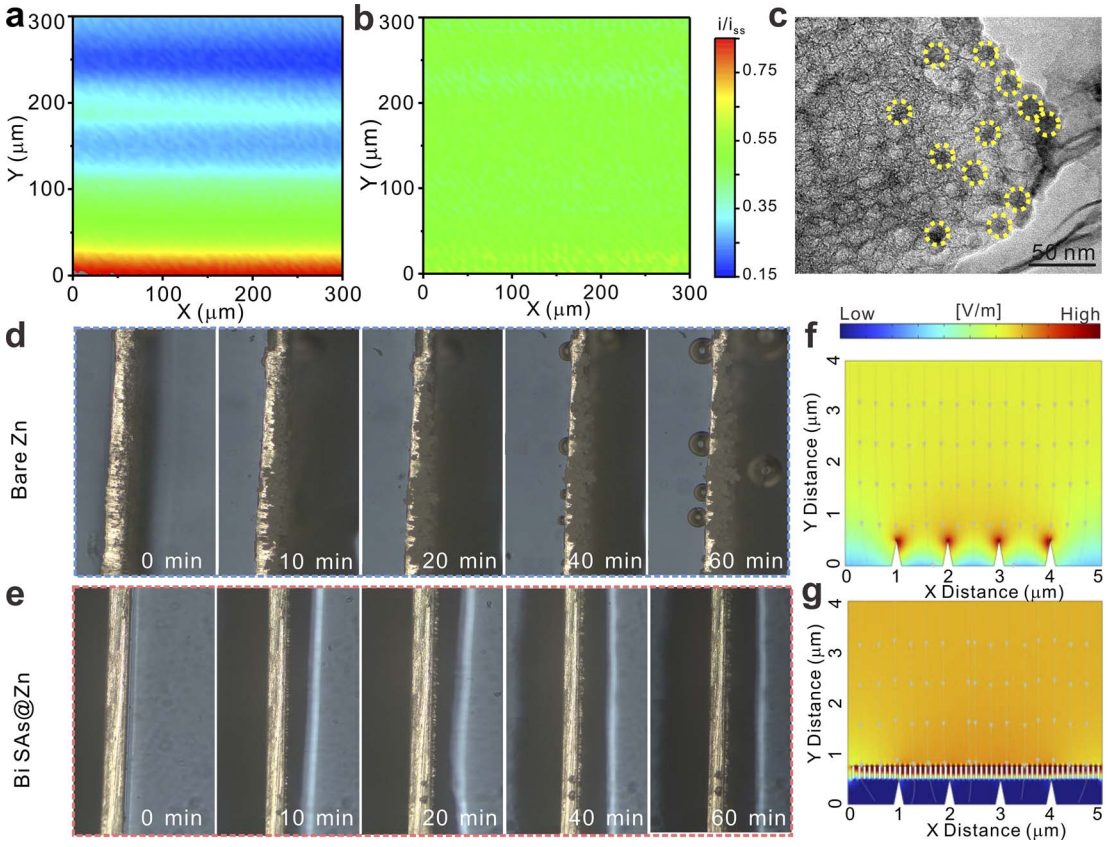

Fig. 4 SECM feedback images of (a) bare Zn and (b) Bi SAs@Zn anodes after zinc deposition for 600 s at 5 mA cm^{-2}. (c) TEM image of Bi SAs@Zn after zinc deposition for 600 s at 5 mA cm^{-2}. *In situ* optical microscope images of (d) bare Zn and (e) Bi SAs@Zn electrodes during Zn plating at 5 mA cm^{-2}. COMSOL electric field simulation of (f) bare Zn and (g) Bi SAs@Zn.

facilitate Zn^{2+} ion transfer (Fig. S19†) by reducing the concentration polarization from 6.2 mV to 3 mV and mitigating ohmic and interfacial electrochemical polarization from 30.88 mV to 23.09 mV. Additionally, *in situ* DRT analysis reveals that the Bi SAs@Zn anode presents a shorter relaxation time during Zn^{2+} deposition (Fig. S20†), indicating that the Bi SAs coating can accelerate the desolvation process of Zn^{2+} ions.[41]

Scanning electrochemical microscopy (SECM) is utilized to probe the surface morphological change of the Zn anode before and after Zn deposition.[43] The local feedback current change reveals that both the bare Zn and Bi SAs@Zn electrodes exhibit a homogeneous surface (Fig. S21†). Following the deposition of Zn, compared to bare Zn, Bi SAs@Zn still provides a uniformly distributed electric field, revealing dense and uniform Zn deposition (Fig. 4a and b). This phenomenon can be also evidenced using scanning electron microscopy (SEM) characterization (Fig. S22†). After 10 min of deposition, Zn nanoparticles with an average size of around 10 nm and a mainly exposed (002) plane are uniformly dispersed on the surface of the Bi SAs (Fig. 4c and S23†). *In situ* optical microscopy observations (Fig. 4d and e) verify that the Bi SAs coating can robustly suppress dendritic growth, while prominent bubbles and dendrites are observed on bare Zn. After 50, 100, and 150 cycles, distinct protruding particles or dendritic structures appear on the bare Zn surface (Fig. S24†), suggesting nonuniform plating/stripping processes and the generation of $Zn_4SO_4(OH)_6 \cdot xH_2O$ byproducts (Fig. S25a†). Conversely, the surface of Bi SAs@Zn appears to be uniform and flat on the whole (Fig. S25b†), reflecting favorable Zn plating/stripping behavior. COMSOL simulations[44,45] illustrate that the Zn^{2+} ions exhibit fluctuations and clustering near the tips of the bare Zn anode surface due to the strong electric field, thus fostering the growth of Zn dendrites (Fig. 4f and S26a†). In stark contrast, the Bi SAs coating can effectively equalize both the Zn^{2+} ionic concentration and electric field, thereby guiding uniform Zn deposition (Fig. 4g and S26b†).

A Bi SAs@Zn//MnO_2 full cell is assembled to further explore the practical applications of the modified zinc anode. A simple precipitation method[46] is employed to synthesize MnO_2 with nanosheet morphology (Fig. S27†). The cyclic voltammetry (CV) curves of the full cells with bare Zn and Bi SAs@Zn anodes exhibit similar shapes (Fig. 5a). However, the Bi SAs@Zn//MnO_2 cell exhibits higher redox current density, suggesting enhanced electrochemical reactivity. This is ascribed to the significantly lower charge transfer resistance of Bi SAs@Zn//MnO_2 (Fig. 5b). The galvanostatic charge–discharge curves verify that the Bi SAs@Zn//MnO_2 cell presents lower voltage hysteresis and higher capacity compared to the Zn//MnO_2 cell (Fig. 5c). The rate performance of the Bi SAs@Zn//MnO_2 cell is also superior to that of the Zn//MnO_2 full cell. When returned to 0.1 A g^{-1}, the Bi SAs@Zn//MnO_2 cell remarkably sustains a capacity of 382 mAh g^{-1} (Fig. 5d). Additionally, the Bi SAs coating is able to

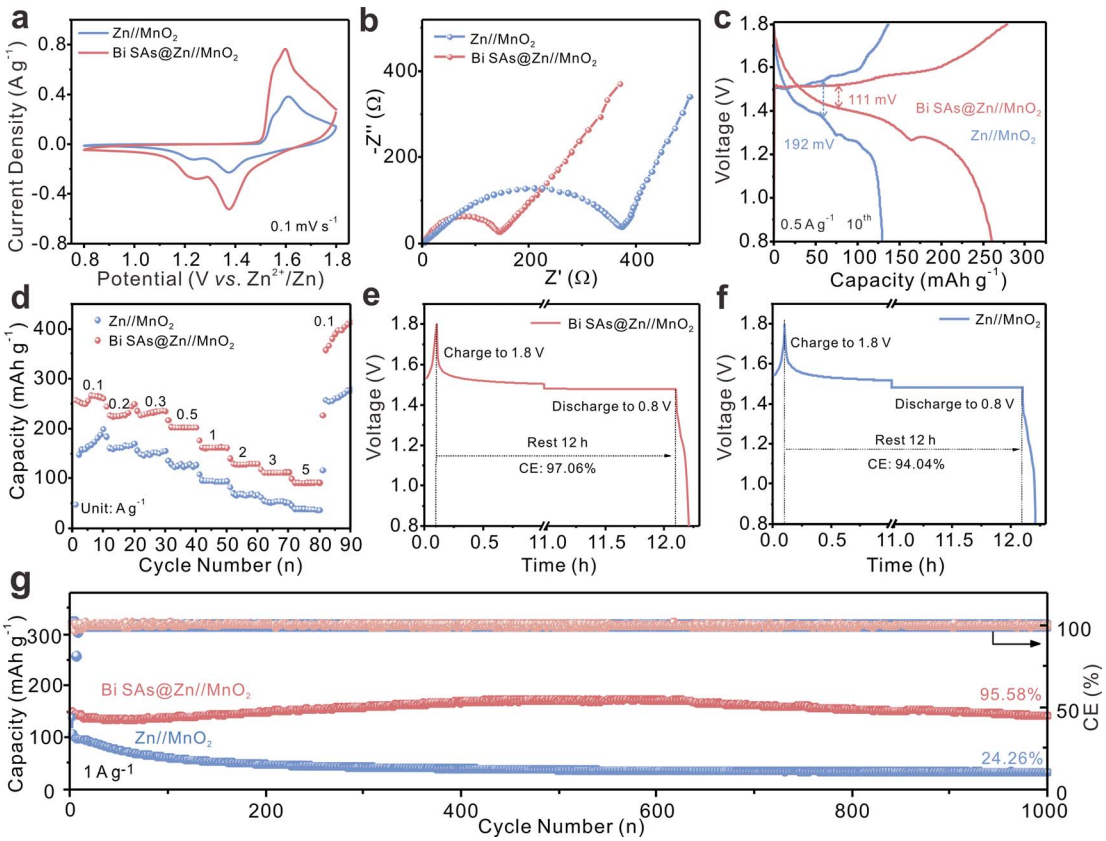

Fig. 5 (a) CV curves at a scan rate of 0.1 mV s^{-1}, (b) EIS plots before cycling, (c) charge/discharge profiles at the 10th cycle with a current density of 0.5 A g^{-1}, and (d) rate performance of Bi SAs@Zn//MnO_2 and Zn//MnO_2 full cells. Self-discharging voltage–time curves of (e) Bi SAs@Zn and (f) bare Zn. (g) Cycling performance of Zn//MnO_2 and Bi SAs@Zn//MnO_2 full cells at 1 A g^{-1}.

mitigate the self-discharge phenomenon in Zn//MnO_2 batteries (Fig. 5e and f), highlighting its ability to alleviate side reactions. The long-term cycling performance of the full cells is evaluated at 1 A g^{-1}. As depicted in Fig. 5g, the Bi SAs@Zn//MnO_2 cell impressively maintains a specific capacity of 150.95 mAh g^{-1} after 1000 cycles with a retention rate of 95.58%. For bare Zn//MnO_2, the capacity fades to 24.26% (35.08 mAh g^{-1}) after 1000 cycles. It is noteworthy that this remarkable cycling stability surpasses those of most reported full cells (Table S3†). Additionally, a full cell using $NH_4V_4O_{10}$ (ref. 47) as cathode also reveals the feasibility of the Bi SAs@Zn anode (Fig. S28 and S29†).

Conclusions

In summary, DFT calculations demonstrated that Bi single atoms incorporated into carbon can act as zincophilic sites and inhibit the HER. It was also predicted that Bi SAs would exhibit stronger binding to Zn foil compared to nitrogen-doped carbon, ensuring the stability of the protective coating. Based on these theoretical predictions, Bi SAs-doped carbon nanobelts are synthesized as a multi-functional protective layer to stabilize a Zn anode. The atomic-scale zincophilic sites can accelerate the desolvation kinetics and migration of Zn^{2+}, promote the uniform distribution of Zn^{2+} to inhibit side reactions, and facilitate rapid dendrite-free Zn deposition. Consequently, the asymmetric cell shows a high average CE of 99.66%, and the symmetric cell exhibits an ultra-long cycle life of 4200 h at a current density/capacity of 5 mA cm^{-2}/1 mAh cm^{-2}. Even at a high deposition capacity/current density of 5 mAh cm^{-2}/20 mA cm^{-2}, the Bi SAs@Zn anode maintains stable cycling over 600 hours with a low overpotential. Furthermore, the Bi SAs@Zn//MnO_2 full cell exhibits outstanding cycling stability at 1 A g^{-1} after 1000 cycles, retaining 95.58% of the initial capacity. This work provides an intriguing strategy to design high-performance Zn anode protection materials at the atomic scale.

Data availability

The data supporting the findings of this study are available within the article and its ESI.† Additional data that support the findings of this study are available from the corresponding author upon reasonable request.

Author contributions

Miaomiao Zhang and Hongyu Wei: investigation, writing-original draft preparation; Yitong Zhou: theoretical calculations; Wendong Wen: formal analysis; Lin Zhang: supervision; Xin-Yao Yu: supervision, writing-review & editing, funding acquisition.

Conflicts of interest

There are no conflicts to declare.

Acknowledgements

This work is supported by supported by the Natural Science Research Project of Universities in Anhui Province (2022AH050121). The Hefei advanced computing center is acknowledged for DFT calculations. We greatly acknowledge Prof. Zhonggang Liu for the help with SECM measurement.

Notes and references

1 Q. Zhang, J. Luan, Y. Tang, X. Ji and H. Wang, Interfacial Design of Dendrite-Free Zinc Anodes for Aqueous Zinc-Ion Batteries, *Angew. Chem., Int. Ed.*, 2020, **59**, 13180–13191.
2 L. Li, Y. Zheng, J. Xu, B. Peng, G. Zhu, J. Wu, L. Ma and Z. Jin, Structural and Interfacial Engineering Strategies for Constructing Dendrite-Free Zinc Metal Anodes, *ACS Energy Lett.*, 2024, 3269–3289.
3 S. Liu, R. Zhang, C. Wang, J. Mao, D. Chao, C. Zhang, S. Zhang and Z. Guo, Zinc ion Batteries: Bridging the Gap from Academia to Industry for Grid-Scale Energy Storage, *Angew. Chem., Int. Ed.*, 2024, **63**, e202400045.
4 S. Bai, Z. Huang, G. Liang, R. Yang, D. Liu, W. Wen, X. Jin, C. Zhi and X. Wang, Electrolyte Additives for Stable Zn Anodes, *Adv. Sci.*, 2024, **11**, 2304549.
5 Y. Zeng, Z. Pei, Y. Guo, D. Luan, X. Gu and X. W. Lou, Zincophilic Interfacial Manipulation against Dendrite Growth and Side Reactions for Stable Zn Metal Anodes, *Angew. Chem., Int. Ed.*, 2023, **62**, e202312145.
6 Y. Zhao, S. Guo, M. Chen, B. Lu, X. Zhang, S. Liang and J. Zhou, Tailoring grain boundary stability of zinc-titanium alloy for long-lasting aqueous zinc batteries, *Nat. Commun.*, 2023, **14**, 7080.
7 Z. Shi, M. Yang, Y. Ren, Y. Wang, J. Guo, J. Yin, F. Lai, W. Zhang, S. Chen, H. N. Alshareef and T. Liu, Highly Reversible Zn Anodes Achieved by Enhancing Ion-Transport Kinetics and Modulating Zn (002) Deposition, *ACS Nano*, 2023, **17**, 21893–21904.
8 N. Dong, F. Zhang and H. Pan, Towards the practical application of Zn metal anodes for mild aqueous rechargeable Zn batteries, *Chem. Sci.*, 2022, **13**, 8243–8252.
9 R. Wang, S. Xin, D. Chao, Z. Liu, J. Wan, P. Xiong, Q. Luo, K. Hua, J. Hao and C. Zhang, Fast and Regulated Zinc Deposition in a Semiconductor Substrate toward High-Performance Aqueous Rechargeable Batteries, *Adv. Funct. Mater.*, 2022, **32**, 2207751.
10 J. Zheng, Q. Zhao, T. Tang, J. Yin, C. D. Quilty, G. D. Renderos, X. Liu, Y. Deng, L. Wang, D. C. Bock, C. Jaye, D. Zhang, E. S. Takeuchi, K. J. Takeuchi, A. C. Marschilok and L. A. Archer, Reversible epitaxial electrodeposition of metals in battery anodes, *Science*, 2019, **366**, 645–648.
11 W. Ling, C. Nie, X. Wu, X.-X. Zeng, F. Mo, Q. Ma, Z. Lu, G. Luo and Y. Huang, Ion Sieve Interface Assisted Zinc Anode with High Zinc Utilization and Ultralong Cycle Life for 61 Wh/kg Mild Aqueous Pouch Battery, *ACS Nano*, 2024, **18**, 5003–5016.

12 Z. Hu, F. Zhang, A. Zhou, X. Hu, Q. Yan, Y. Liu, F. Arshad, Z. Li, R. Chen, F. Wu and L. Li, Highly Reversible Zn Metal Anodes Enabled by Increased Nucleation Overpotential, *Nano-Micro Lett.*, 2023, **15**, 171.

13 Y. Zeng, P. X. Sun, Z. Pei, Q. Jin, X. Zhang, L. Yu and X. W. Lou, Nitrogen-Doped Carbon Fibers Embedded with Zincophilic Cu Nanoboxes for Stable Zn-Metal Anodes, *Adv. Mater.*, 2022, **34**, 2200342.

14 Y. Liang, M. Qiu, P. Sun and W. Mai, Comprehensive Review of Electrolyte Modification Strategies for Stabilizing Zn Metal Anodes, *Adv. Funct. Mater.*, 2023, **33**, 2304878.

15 Y. Wang, Z. Wang, W. K. Pang, W. Lie, J. A. Yuwono, G. Liang, S. Liu, A. M. D. Angelo, J. Deng, Y. Fan, K. Davey, B. Li and Z. Guo, Solvent control of water O–H bonds for highly reversible zinc ion batteries, *Nat. Commun.*, 2023, **14**, 2720.

16 Q. Liu, X. Liu, Y. Liu, M. Huang, W. Wang, Y. Cheng, H. Zhang and L. Xu, Atomic-Level Customization of Zinc Crystallization Kinetics at the Interface for High-Utilization Zn Anodes, *ACS Nano*, 2024, **18**, 4932–4943.

17 X. Shen, W. Chen, H. Wang, L. Zhang, B. Hao, C. Zhu, X. Yang, M. Sun, J. Zhou, X. Liu, C. Yan and T. Qian, Selectively "size-excluding" water molecules to enable a highly reversible zinc metal anode, *Chem. Sci.*, 2024, **15**, 10182–10192.

18 D. Zhang, Z. Song, L. Miao, Y. Lv, L. Gan and M. Liu, In situ Nafion-nanofilm oriented (002) Zn electrodeposition for long-term zinc-ion batteries, *Chem. Sci.*, 2024, **15**, 4322–4330.

19 J. Li, D. Röhrens, G. Dalfollo, X. Wu, Z. Lu, Q. Gao, B. Han, R. Sun, C. Zhou, J. Wang and Z. Cai, Low-temperature replacement construction of three-dimensional corrosion-resistant interface for deeply rechargeable Zn metal batteries, *Nano Mater. Sci.*, 2024, **6**, 329–336.

20 J. Zhou, M. Xie, F. Wu, Y. Mei, Y. Hao, R. Huang, G. Wei, A. Liu, L. Li and R. Chen, Ultrathin Surface Coating of Nitrogen-Doped Graphene Enables Stable Zinc Anodes for Aqueous Zinc-Ion Batteries, *Adv. Mater.*, 2021, **33**, 2101649.

21 D. Wang, H. Liu, D. Lv, C. Wang, J. Yang and Y. Qian, Rational Screening of Artificial Solid Electrolyte Interphases on Zn for Ultrahigh-Rate and Long-Life Aqueous Batteries, *Adv. Mater.*, 2023, **35**, 2207908.

22 L. Li, S.-F. Jia, M.-H. Cao, Y.-Q. Ji, H.-W. Qiu and D. Zhang, Progress in research on metal-based materials in stabilized Zn anodes, *Rare Met.*, 2024, **43**, 20–40.

23 Y. Xiang, L. Zhou, P. Tan, S. Dai, Y. Wang, S. Bao, Y. Lu, Y. Jiang, M. Xu and X. Zhang, Continuous Amorphous Metal–Organic Frameworks Layer Boosts the Performance of Metal Anodes, *ACS Nano*, 2023, **17**, 19275–19287.

24 G. Zhu, H. Zhang, J. Lu, Y. Hou, P. Liu, S. Dong, H. Pang and Y. Zhang, 3D Printing of MXene-Enhanced Ferroelectric Polymer for Ultrastable Zinc Anodes, *Adv. Funct. Mater.*, 2024, **34**, 2305550.

25 L. He, Q. Zhang, H. Li, S. Liu, T. Cheng, R. Zhang, Y. Wang, P. Zhang and Z. Shi, Construction of Phosphorus-Functionalized Multichannel Carbon Interlayers for Dendrite-Free Metallic Zn Anodes, *Energy Environ. Mater.*, 2024, **7**, e12689.

26 M. Li, Q. He, Z. Li, Q. Li, Y. Zhang, J. Meng, X. Liu, S. Li, B. Wu, L. Chen, Z. Liu, W. Luo, C. Han and L. Mai, A Novel Dendrite-Free Mn^{2+}/Zn^{2+} Hybrid Battery with 2.3 V Voltage Window and 11000-Cycle Lifespan, *Adv. Energy Mater.*, 2019, **9**, 1901469.

27 C.-Q. Chao, Y.-N. Li and Y. Zhao, Application of carbon materials for Zn anode protection in aqueous Zn metal batteries, *Rare Met.*, 2024, **43**, 4807–4843.

28 B. Tang, Y. Zhou, Q. Ji, Z. Zhuang, L. Zhang, C. Wang, H. Hu, H. Wang, B. Mei, F. Song, S. Yang, B. M. Weckhuysen, H. Tan, D. Wang and W. Yan, A Janus dual-atom catalyst for electrocatalytic oxygen reduction and evolution, *Nat. Synth.*, 2024, **3**, 878–890.

29 P. Yan, T. Yang, M. Lin, Y. Guo, Z. Qi, Q. Luo and X.-Y. Yu, "One Stone Five Birds" Plasma Activation Strategy Synergistic with Ru Single Atoms Doping Boosting the Hydrogen Evolution Performance of Metal Hydroxide, *Adv. Funct. Mater.*, 2023, **33**, 2301343.

30 Z. Yang, Y. Dang, P. Zhai, Y. Wei, Q. Chen, J. Zuo, X. Gu, Y. Yao, X. Wang, F. Zhao, J. Wang, S. Yang, P. Tang and Y. Gong, Single-Atom Reversible Lithiophilic Sites toward Stable Lithium Anodes, *Adv. Energy Mater.*, 2022, **12**, 2103368.

31 D. Qiu, W. Zhao, B. Zhang, M. T. Ahsan, Y. Wang, L. Zhang, X. Yang and Y. Hou, Ni-Single Atoms Modification Enabled Kinetics Enhanced and Ultra-Stable Hard Carbon Anode for Sodium-Ion Batteries, *Adv. Energy Mater.*, 2024, **14**, 2400002.

32 K. Xu, M. Zhu, X. Wu, J. Liang, Y. Liu, T. Zhang, Y. Zhu and Y. Qian, Dendrite-tamed deposition kinetics using single-atom Zn sites for Li metal anode, *Energy Storage Mater.*, 2019, **23**, 587–593.

33 W. Huang, S. Liu, R. Yu, L. Zhou, Z. Liu and L. Mai, Single-Atom Lithiophilic Sites Confined within Ordered Porous Carbon for Ultrastable Lithium Metal Anodes, *Energy Environ. Mater.*, 2023, **6**, e12466.

34 C. Zhang, J. Xie, C. Zhao, Y. Yang, Q. An, Z. Mei, Q. Xu, Y. Ding, G. Zhao and H. Guo, Regulating the Lithium Ions' Local Coordination Environment through Designing a COF with Single Atomic Co Site to Achieve Dendrite-Free Lithium-Metal Batteries, *Adv. Mater.*, 2023, **35**, 2304511.

35 Y. Zeng, Z. Pei, D. Luan and X. W. Lou, Atomically Dispersed Zincophilic Sites in N,P-Codoped Carbon Macroporous Fibers Enable Efficient Zn Metal Anodes, *J. Am. Chem. Soc.*, 2023, **145**, 12333–12341.

36 S. Chen, J. Chen, X. Liao, Y. Li, W. Wang, R. Huang, T. Zhao, S. Yan, Z. Yan, F. Cheng and H. Wang, Enabling Low-Temperature and High-Rate Zn Metal Batteries by Activating Zn Nucleation with Single-Atomic Sites, *ACS Energy Lett.*, 2022, **7**, 4028–4035.

37 Z. Yang, F. Lai, Q. Mao, C. Liu, R. Wang, Z. Lu, T. Zhang and X. Liu, Reversing Zincophobic/Hydrophilic Nature of Metal-N-C via Metal-Coordination Interaction for Dendrite-Free Zn Anode with High Depth-of-Discharge, *Adv. Mater.*, 2024, **36**, 2311637.

38 K. Lee, E. J. Kim, J. Kim, K. H. Kim, Y. J. Lee, M. J. Lee, K. Ryu, S. Shin, J. Choi, S. H. Kwon, H. Lee, J. K. Kim, B.-H. Kim,

B. J. Kim, S. W. Lee and N. Coordination Engineering of, O Co-Doped Cu Single Atom on Porous Carbon for High Performance Zinc Metal Anodes, *Adv. Energy Mater.*, 2024, **14**, 2303803.

39 Z. Cao, R. Ma, X. Xiao, D. Xiong, W. Yi, S. Tao, Z. Song, Y. Xiong, W. Deng, J. Hu, H. Hou, X. Ji and G. Zou, Single atom vacancy engineering with highly reversible N_4 sites enable ultra-low overpotential for durable zinc-ion supercapacitors, *Energy Storage Mater.*, 2024, **66**, 103189.

40 E. Zhang, T. Wang, K. Yu, J. Liu, W. Chen, A. Li, H. Rong, R. Lin, S. Ji, X. Zheng, Y. Wang, L. Zheng, C. Chen, D. Wang, J. Zhang and Y. Li, Bismuth Single Atoms Resulting from Transformation of Metal–Organic Frameworks and Their Use as Electrocatalysts for CO_2 Reduction, *J. Am. Chem. Soc.*, 2019, **141**, 16569–16573.

41 L. Wang, B. Zhang, W. Zhou, Z. Zhao, X. Liu, R. Zhao, Z. Sun, H. Li, X. Wang, T. Zhang, H. Jin, W. Li, A. Elzatahry, Y. Hassan, H. J. Fan, D. Zhao and D. Chao, Tandem Chemistry with Janus Mesopores Accelerator for Efficient Aqueous Batteries, *J. Am. Chem. Soc.*, 2024, **146**, 6199–6208.

42 K. Liu, M. Sun, S. Yang, G. Gan, S. Bu, A. Zhu, D. Lin, T. Zhang, C. Luan, C. Zhi, P. Wang, B. Huang, G. Hong and W. Zhang, Multifunctional Nanodiamond Interfacial Layer for Ultra-Stable Zinc-Metal Anodes, *Adv. Energy Mater.*, 2024, **14**, 2401479.

43 M. Peng, X. Tang, K. Xiao, T. Hu, K. Yuan and Y. Chen, Polycation-Regulated Electrolyte and Interfacial Electric Fields for Stable Zinc Metal Batteries, *Angew. Chem., Int. Ed.*, 2023, **62**, e202302701.

44 M. Liu, W. Yuan, G. Ma, K. Qiu, X. Nie, Y. Liu, S. Shen and N. Zhang, In-Situ Integration of a Hydrophobic and Fast-Zn^{2+}-Conductive Inorganic Interphase to Stabilize Zn Metal Anodes, *Angew. Chem., Int. Ed.*, 2023, **62**, e202304444.

45 B. Wei, J. Zheng, Abhishek, X. Liu, J. Wu, Z. Qi, Z. Hou, R. Wang, J. Ma, A. N. Gandi, Z. Wang and H. Liang, Design Principle of Insulating Surface Protective Layers for Metallic Zn Anodes: A Case Study of ZrO_2, *Adv. Energy Mater.*, 2024, **14**, 2401018.

46 T. Xiong, Z. G. Yu, H. Wu, Y. Du, Q. Xie, J. Chen, Y.-W. Zhang, S. J. Pennycook, W. S. V. Lee and J. Xue, Defect Engineering of Oxygen-Deficient Manganese Oxide to Achieve High-Performing Aqueous Zinc Ion Battery, *Adv. Energy Mater.*, 2019, **9**, 1803815.

47 D. Li, Y. Tang, S. Liang, B. Lu, G. Chen and J. Zhou, Self-assembled multilayers direct a buffer interphase for long-life aqueous zinc-ion batteries, *Energy Environ. Sci.*, 2023, **16**, 3381–3390.